Ceramics International 44 (2018) 17953–17961

Contents lists available at ScienceDirect

Ceramics International

journal homepage: www.elsevier.com/locate/ceramint

A comparative study of photocatalytically active nanocrystalline tetragonal zyrcon-type and monoclinic scheelite-type bismuth vanadate

Slobodan D. Dolić[a], Dragana J. Jovanović[a,*], Krisjanis Smits[b], Biljana Babić[c], Milena Marinović-Cincović[a], Slavica Porobić[a], Miroslav D. Dramićanin[a]

[a] Vinča Institute of Nuclear Sciences, University of Belgrade, P.O. Box 522, 11001 Belgrade, Serbia
[b] Institute of Solid State Physics, University of Latvia, 8 Kengaraga Street, Riga, LV-1063, Latvia
[c] Institute of Physics Belgrade, University of Belgrade, Pregrevica 118, 11000 Belgrade, Serbia

ARTICLE INFO

Keywords:
Bismuth vanadate
Tetragonal zircon-type $BiVO_4$
Monoclinic scheelite-type $BiVO_4$
Photocatalysis
Methyl orange degradation

ABSTRACT

Monoclinic scheelite-type $BiVO_4$ is currently considered as one of the most promising non-titania photocatalysts, wheras tetragonal zircon-type $BiVO_4$ is still poorly understood. Herein, a new and simple synthetic approach was applied and nanostructured single-phase zircon-type $BiVO_4$ was successfully prepared by a controllable ethylene-glycol colloidal route. In addition, nanostructured monoclinic scheelite-type $BiVO_4$ powders were also fabricated through annealing of the as-prepared samples. A comparative study of the two $BiVO_4$ polymorphs was conducted and it turned out that the novel synthetic approach had a significant impact on porosity and photocatalytic performance of zircon-structured $BiVO_4$. All the prepared materials, as-prepared and annealed, were mesoporous, while measured values of specific surface area of some zircon-structured samples ($\sim 34\ m^2/g$) were ~ 7 times higher than those reported thus far for this phase. Interestingly, for the first time, zircon-type $BiVO_4$, previously considered to be a poor photocatalyst, exhibited a better overall performance in degradation of methyl orange compared to monoclinic scheelite-type $BiVO_4$. Hence, it could be expected that the here-presented synthesis and observations will both arouse interest in scarcely studied tetragonal zircon-type $BiVO_4$ and facilitate as well as speed up further research of its properties.

1. Introduction

As solar energy is the most abundant energy source, harvesting energy directly from sunlight over semiconducting nanomaterials offers a very attractive approach to resolve both the potential energy crisis and problems of environmental pollution. Among non-titania (TiO_2)-based visible-light driven photocatalysts, considerable research has been devoted to bismuth vanadate ($BiVO_4$) [1–4]. Mainly, studies have focused on monoclinic $BiVO_4$ and it has proved to be an excellent material for use (under visible-light illumination) in photocatalytic water splitting and photocatalytic degradation of organic compounds (air/water pollutants) [1–7].

$BiVO_4$ is polymorphous and occurs naturally as three crystalline forms: orthorhombic pucherite (*op*-$BiVO_4$), tetragonal dreyerite (*tz*-$BiVO_4$, zircon-type structure, space group *I*41/amd), and monoclinic clinobisvanite (*ms*-$BiVO_4$, distorted scheelite-type structure, space group I2/b). Synthetic $BiVO_4$, apart from crystallizing in dreyerite and clinobisvanite structures, also appears in tetragonal phase (*ts*-$BiVO_4$, scheelite-type structure, space group I41/a). Pucherite is an unstable phase and is never obtained in laboratory [1,8].

$BiVO_4$-based ceramics have been intensively studied because of semiconductivity, ion conductivity, photocatalytic behavior, dielectric properties, ferroelastic-paraelastic phase transition and pigmentation. Brilliant yellow color of non-toxic *ms*-$BiVO_4$ makes it a good commercially available substitute for toxic cadmium- and lead-based yellow pigments. All crystalline phases of synthetic $BiVO_4$, *ts*-$BiVO_4$, *ms*-$BiVO_4$ and *tz*-$BiVO_4$, are n-type semiconductors with respective band gap energies of 2.34, 2.40, and 2.90 eV [1,3]. Their thermodynamic stability varies in the order *ms*-$BiVO_4$, *ts*-$BiVO_4$, *tz*-$BiVO_4$, with *ms*-$BiVO_4$ being the most stable phase. A phase transition from *tz*-$BiVO_4$ to *ms*-$BiVO_4$ takes place irreversibly upon heating to 397–497 °C; thus, *tz*-$BiVO_4$ is generally synthesized at lower temperatures. At 255 °C $BiVO_4$ undergoes a reversible *ms*-$BiVO_4$-to-*ts*-$BiVO_4$ phase transition [1].

With a focus on catalysis many processes and preparative conditions have been employed to prepare *ms*-$BiVO_4$ micro- and nanoparticles of varying morphologies and sizes [1–3,8–10]. At the same time, few approaches were attempted for synthesis of the zircon-structured phase in aqueous media by the low-temperature process: a precipitation

* Corresponding author.
E-mail address: draganaj@vinca.rs (D.J. Jovanović).

https://doi.org/10.1016/j.ceramint.2018.06.272
Received 30 May 2018; Accepted 29 June 2018
Available online 30 June 2018

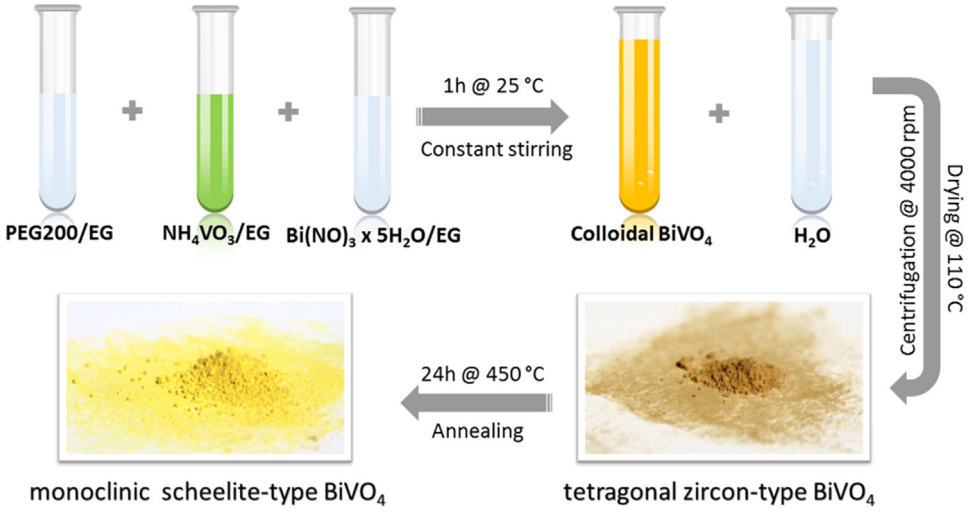

Fig. 1. A general synthetic scheme for preparing *tz*- $BiVO_4$ and *ms*-$BiVO_4$ nanoparticles.

method from a $Bi(NO_3)_3$ nitric acid solution and an aqueous NH_4VO_3 solution at room temperature [8,9,11–13], a precipitation from Bi_2O_3 and V_2O_5 in an aqueous nitric acid solution at room temperature [10], a hydrothermal method [6,14,15], and a rapid microwave-assisted aqueous process [16]. Also, rather few nanostructured zircon-type $BiVO_4$ were made: small ellipsoidal nanoparticles of about 20 nm [9], nanoparticles with diameters in a range 10–40 nm [13], and nanoparticles with diameters of around 10–20 nm [16].

It is well-known for *ms*-$BiVO_4$ to exhibit excellent photocatalytic activity under visible light [1–7]. Compared with *ms*-$BiVO_4$, *ts*-$BiVO_4$ is much less studied and appears to display moderate photocatalytic activity [9] although first studies declared it to be a poor photocatalyst [10,12]. On the other hand, rather few photocatalytic studies concern pure *tz*-$BiVO_4$ and it was found to be a poor (or, even inactive) photocatalyst [9,10,13–16]. Observe, however, that enhanced photocatalytic performance has been reported for a number of doped (chemically *impure*) $BiVO_4$ materials with a zircon-type structure [1–3].

Although more than 1000 research papers in the open literature have been devoted to $BiVO_4$ over the past decade, yet two dozen or so of them consider its zircon-type structure at any length. As suggested in [11] this could be due to its not-so-simple synthesis by conventional synthetic routes. More probably, however, its lower visible-light absorption (compared with *ms*-$BiVO_4$) may have deemed *tz*-$BiVO_4$ a less interesting material. Several reports of its poor photocatalytic performance only reinforced this view. Nevertheless, zircon-structured $BiVO_4$ (with a band gap of 2.9 eV) still absorbs more visible light than TiO_2 (3.2 eV for anatase)-the most widely used and most intensely studied photocatalyst. Whatever the reason, *tz*-$BiVO_4$ has not been sufficiently studied so far, and, in particular, new approaches to its preparation and better understanding of nanocrystalline *tz*-$BiVO_4$ are needed and would be of significance.

In this paper, in an attempt to address before-mentioned gaps in the literature, we aimed to develop a novel and suitable low-temperature synthesis of nanostructured single-phase tetragonal zircon-type $BiVO_4$ in non-aqueous medium. In order to prepare powdered nanocrystalline *tz*-$BiVO_4$, an ethylene-glycol colloidal route at room temperature was utilized. Moreover, as a consequence of the irreversible tetragonal-to-monoclinic transition, monoclinic scheelite-type $BiVO_4$ could be easily obtained by thermal treatment of as-prepared powders. Further, we aimed to determine whether or not (and to what extent) the new synthetic approach to *tz*-$BiVO_4$ influenced its adsorption and/or photocatalytic performance. To do so, the selectively prepared scheelite-type $BiVO_4$ lended itself readily to comparison and a comparative study of two $BiVO_4$ polymorphs was carried out. To assess eventual influence, photocatalytic activity for both *tz*-$BiVO_4$ and *ms*-$BiVO_4$ was evaluated by degradation of methyl orange in an aqueous solution under sun-like illumination.

2. Experimental

2.1. Preparation of *tz*-$BiVO_4$ and *ms*-$BiVO_4$ nanoparticles

Colloidal $BiVO_4$ samples were synthesized by ethylene glycol-mediated colloidal route at room temperature. Powders of *tz*-$BiVO_4$ were made from the previously prepared $BiVO_4$ colloids, while powders of *ms*-$BiVO_4$ were obtained by annealing the *tz*-$BiVO_4$ at 450 °C for 24 h. Therefore, the tetragonal and monoclinic $BiVO_4$ crystallites can be selectively prepared in this process simply by adjusting the calcining temperature.

All chemicals were of highest purity commercially available and were used as received without further purification. These included: $Bi(NO_3)_3 \times 5H_2O$ (Sigma-Aldrich, 97%), NH_4VO_3 (Alfa Aesar, 99.999%), ethylene glycol (Sigma-Aldrich, 97%), polyethylene glycol 200 (PEG-200, Alfa Aesar), HNO_3 (J.T. Baker, 65%) and distilled water.

In a typical synthesis of colloidal $BiVO_4$, stoichiometric amounts of NH_4VO_3, $Bi(NO_3)_3 \times 5H_2O$ and PEG-200, were separately dissolved in ethylene glycol. In this way, the 0.075 M, 0.050 M and 0.025 M ethylene glycol solutions of both precursors, NH_4VO_3 and $Bi(NO_3)_3 \times {}_5H_2O$, were prepared. Then, the ethylene glycol solution of PEG-200 was slowly added drop-wise into the solution of NH_4VO_3 and the resulting mixture was left under vigorous stirring for 30 min. At the same time, 200 μL of HNO_3 was added to the bismuth precursor solution. After 30 min of stirring, the bismuth precursor solution was slowly added drop-wise into the mixture of NH_4VO_3 and PEG-200 and left under vigorous stirring for 1 h. Finally, orange-yellow colloids of $BiVO_4$ were obtained (Fig. 1).

In order to prepare powders of $BiVO_4$, the colloids made as described above were additionally treated. This treatment involved mixing of certain amounts of colloidal $BiVO_4$ with 5 times the amount of distilled water. A formed precipitate of $BiVO_4$ particles was then separated from the obtained mixture by centrifugation (15 min @ 4000 rpm), and the collected precipitate was washed several times with water and dried in an oven at 110 °C for 24 h. The resulting yellowish-brown powders of $BiVO_4$ were thoroughly characterized by a wide variety of methods. The samples, respectively corresponding to precursor concentrations of 0.075 M, 0.050 M, and 0.025 M, exhibited pure *tz*- $BiVO_4$ structure and they are referred to as 1, 1A and 1B.

A second series of samples was synthesized as follows. The *tz*-$BiVO_4$

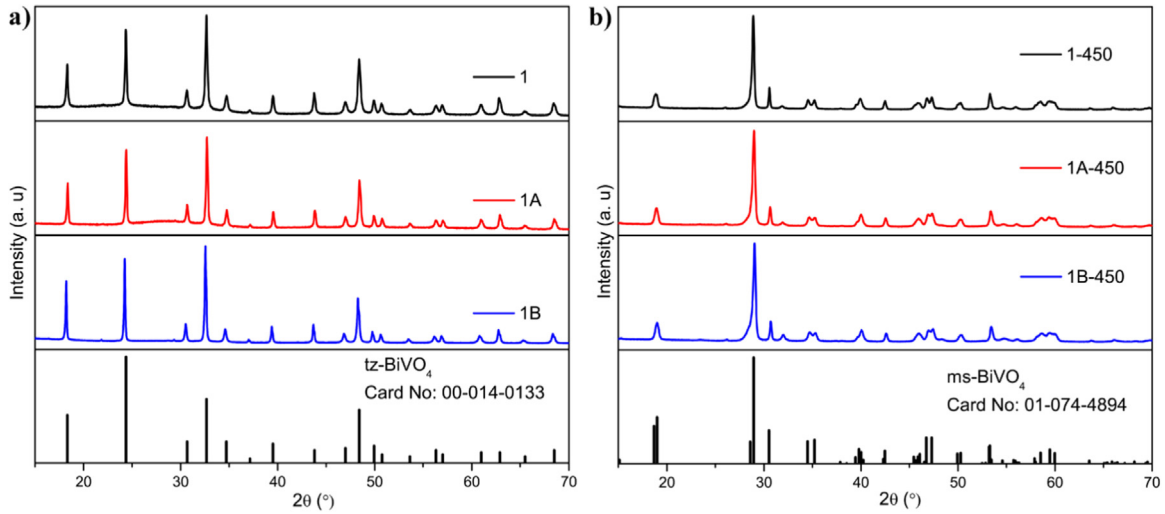

Fig. 2. XRD patterns of: a) *tz*-$BiVO_4$ and b) *ms*-$BiVO_4$ powders.

powders were annealed in air at 450 °C for 24 h and yellow-orange powders (labeled as 1–450, 1A-450, and 1B-450) were obtained. These powders were subjected to detailed characterization studies and it was shown that they exhibit the monoclinic scheelite-type structure (*ms*-$BiVO_4$).

2.2. Instrumentation

Crystalline structure of the samples was examined by powder X-ray diffraction (XRD) measurements on a Rigaku SmartLab diffractometer using Cu-Ka radiation (λ = 0.15405 nm). Diffraction data were recorded with a step size of 0.02° and a counting time of 0.7°/min over the angular range 2θ from 10 ° to 100 °. Transmission electron microscopy (TEM) studies were done on a Tecnai G20 (FEI) system operating at an accelerating voltage of 200 kV. The samples were placed on a perforated carbon film (S147-4, Agar scientific) and dried in air for 24 h. It was observed that at high doses of electron radiation defects were induced into the crystals until their crystalline structure disappeared. Hence, for HRTEM images the electron beam intensity was strongly reduced by inserting a condenser aperture and by decreasing the spot size. Diffuse reflection spectra measurements were recorded with 1 nm resolution on a Shimadzu UV–Visible UV-2600 (Shimadzu Corporation, Japan) spectrophotometer equipped with an integrated sphere (ISR-2600 Plus (for UV-2600)) in the range from 350 nm to 800 nm. FTIR spectroscopy measurements were performed on Nicolet TM 380 FT-IR spectrometer with Smart Orbit ATR accessory (Thermo Electron Corporation, Madison, U.S.A). Brunauer–Emmett–Teller (BET) surface area and porosity measurements were carried out by N_2 adsorption at −196 °C using Surfer (Thermo Fisher Scientific, USA). The pore size distribution was estimated by applying the Barrett-Joyner-Halenda method to desorption branch of isotherms, while mesopore surface and micropore volume were estimated using the t-plot method [17,18]. The thermal stability of the samples was investigated by simultaneous non-isothermal thermo-gravimetric analysis (TG) and differential thermal analysis (DTA) using a Setaram Setsys Evolution 1750 instrument. The measurements were performed on powder samples (*cca.* 10 mg each) at a heating rate of 10 °C/min, in dynamic nitrogen atmosphere with a gas flow rate of 20 ml/min, and in the temperature range of 30–900 °C.

2.3. Photocatalytic and adsorption test

Methyl orange (MO), anionic and water soluble azo dye, was used as a representative dye pollutant to evaluate photocatalytic activity of our $BiVO_4$ samples. Removal of MO in aqueous solutions was carried out in an immersion-type cylindrical photochemical reactor (with an inner diameter of 10 cm and 12 cm in height). Adsorption experiments were carried out in the dark before subsequent photocatalytic experiments with light illumination. In photodegradation experiments a suspension of $BiVO_4$ catalyst powder and MO dye was exposed to artificial light from Osram Ultra-Vitalux 300 W lamp (radiated power 315–400 nm (UVA) = 13.6 W; radiated power 280–315 nm (UVB) = 3.0 W) placed 15 cm above the reactor. Temperature was maintained at 18 °C by continuous flow of water through the reactor during the experiments. In a typical test, MO was dissolved in 200 ml of deionized water to make a 5 mg/L solution. Catalyst concentration was 1 g/L.

During adsorption/photocatalytic experiments, MO dye solution with $BiVO_4$ catalyst powder was continuously magnetically stirred, and, at appropriate time intervals, fixed amounts of the suspension were collected. The MO concentration was monitored over time by tracking the change of absorbance at a wavelength of 464 nm using the UV–Vis absorption spectrophotometer. Prior to light illumination, the photocatalyst/MO suspension was stirred in dark for 180 min to ensure adsorption-desorption equilibrium.

3. Results and discussion

Two series of samples were prepared and characterized: the as-prepared *tz*-$BiVO_4$ samples, respectively corresponding to precursor concentrations of 0.075 M, 0.050 M, and 0.025 M, and referred to as 1, 1A and 1B. The samples annealed at 450 °C (*ms*-BiVO4) are labeled as 1-450, 1A-450, and 1B-450 (see Experimental Section).

3.1. Structural and microstructural properties of *tz*-$BiVO_4$ and *ms*-$BiVO_4$ nanoparticles

X-ray diffraction patterns of the as-prepared and annealed powders, respectively, are shown in Fig. 2, while structural details are given in Table 1. As it will be seen, the samples crystallize either in a zircon-type tetragonal or in a scheelite-type monoclinic structure. XRD patterns given in Fig. 2a clearly show the presence of a single tetragonal zircon-type phase (space group *I*41/amd, card No. 00-014-0133) and no peaks from any other phase or impurity. Similarly, patterns of the annealed powders (Fig. 2b) reveal the presence of a pure single monoclinic scheelite-type phase (space group: I2/b, card No. 01-074-4894).

The absence of impurities and very small shift of reflections compared to the reflection positions of bulk $BiVO_4$ indicate that nanoparticles were successfully synthesized. In addition, relatively intense

Table 1
Structural parameters of *tz*-$BiVO_4$ and *ms*-$BiVO_4$ nanoparticles.

	tz-$BiVO_4$			*ms*-$BiVO_4$		
Sample	**1**	**1A**	**1B**	**1-450**	**1A-450**	**1B-450**
Crystallite size (nm)	9.4	4.0	4.3	21.1	16.3	16.5
a (Å)	7.31	7.30	7.30	5.19	5.18	5.18
b (Å)	7.31	7.30	7.30	5.11	5.10	5.10
c (Å)	6.49	6.47	6.47	11.70	11.70	11.69
V (Å^3)	346.80	344.79	344.79	310.29	309.09	308.83

reflection peaks suggest that the as-synthesized nanoparticles were highly crystalline, and no additional thermal treatment was required to produce *tz*-$BiVO_4$. However, in order to obtain the *ms*-$BiVO_4$ nanoparticles, the as-synthesized samples had to be annealed at 450∘C. The average crystallite sizes of 4–9.4 nm for *tz*-$BiVO_4$ and 16.3–21 nm for *ms*-$BiVO_4$ were estimated from the diffraction peaks by the Halder–Wagner method (see Table 1).

Representative HRTEM images (for both low and high magnifications) of *tz*-$BiVO_4$-1A and *ms*-$BiVO_4$-1A nanoparticles are presented in Fig. 3. These images show nanocrystals in sizes of 5–10 nm in the case of *tz*-$BiVO_4$ and larger polycrystalline particles in range of 20–60 nm for *ms*-$BiVO_4$. These estimates are somewhat consistent with the crystallite sizes evaluated from the powder XRD measurements.

3.2. Thermal properties of *tz*-$BiVO_4$ and *ms*-$BiVO_4$ nanoparticles

The TGA-DTA analysis was used to find optimal calcination temperature and to determine the phase changes between *tz*-$BiVO_4$ and *ms*-$BiVO_4$, while DSC was used to see main differences between the DSC curves for *tz*-$BiVO_4$ and *ms*-$BiVO_4$ nanoparticles. Thermal degradation properties of *tz*-$BiVO_4$-1A nanoparticles are given in Fig. 4. The results of the TGA-DTA analysis of all samples corresponded to the classical thermal behavior of $BiVO_4$ [19]. There is no significant weight loss in the TGA curve of $BiVO_4$. It could be roughly generalized that the TGA decomposition of $BiVO_4$ consists of four-stage weight loss at temperatures in the range of about 30–100 °C, 100–270 °C, 270–550 °C and 550–900 °C. The first stage of weight loss for the sample was 0.68%, second 2.12%, third 1.27% and fourth 0.54%. The total mass loss in the TGA of *tz*-$BiVO_4$-1A sample was about 4.6%. The DTA curves contain 4

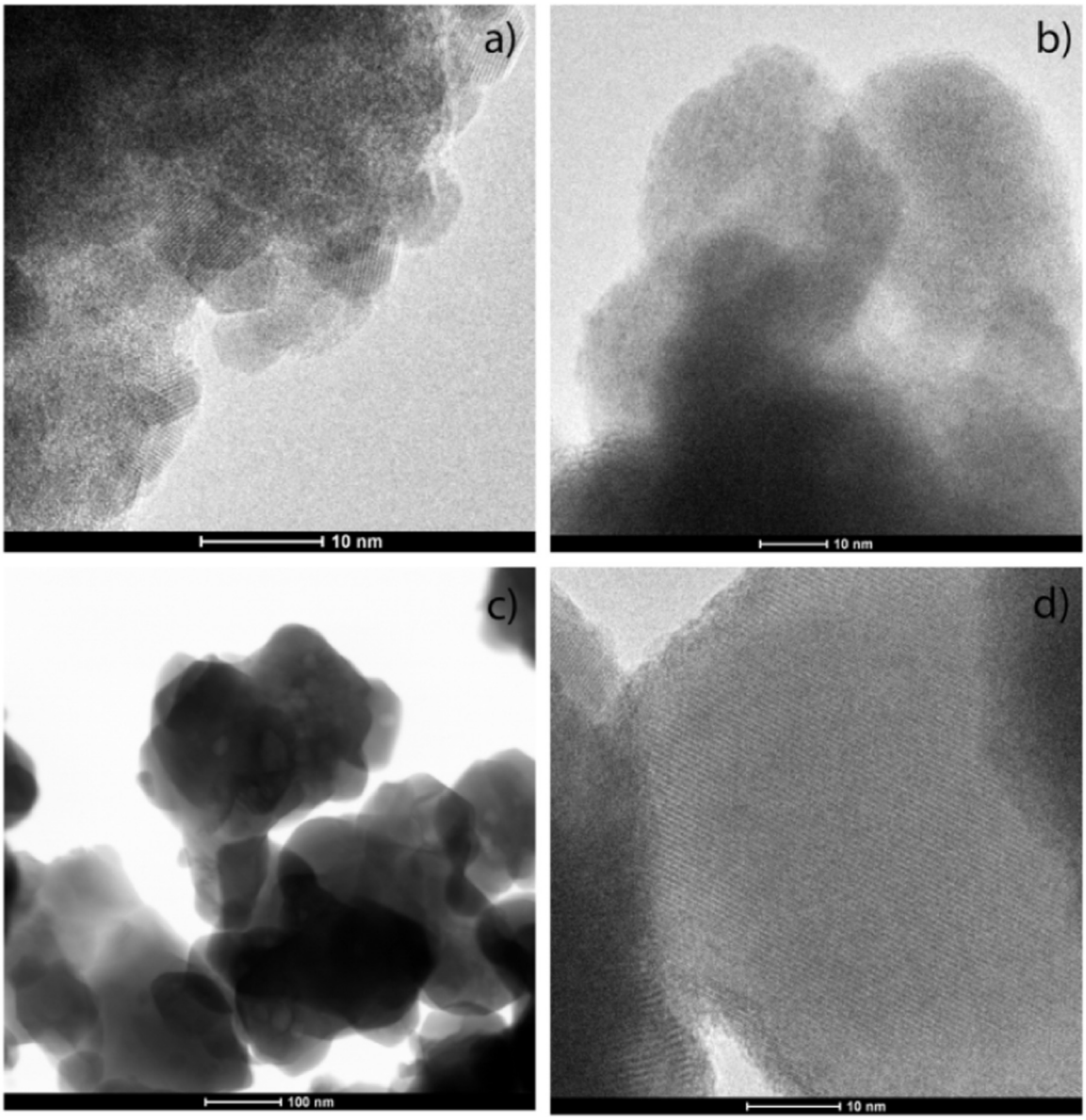

Fig. 3. TEM images of: *tz*-$BiVO_4$-1A (a, b) and *ms*-$BiVO_4$-1A (c, d) nanoparticles at different magnifications.

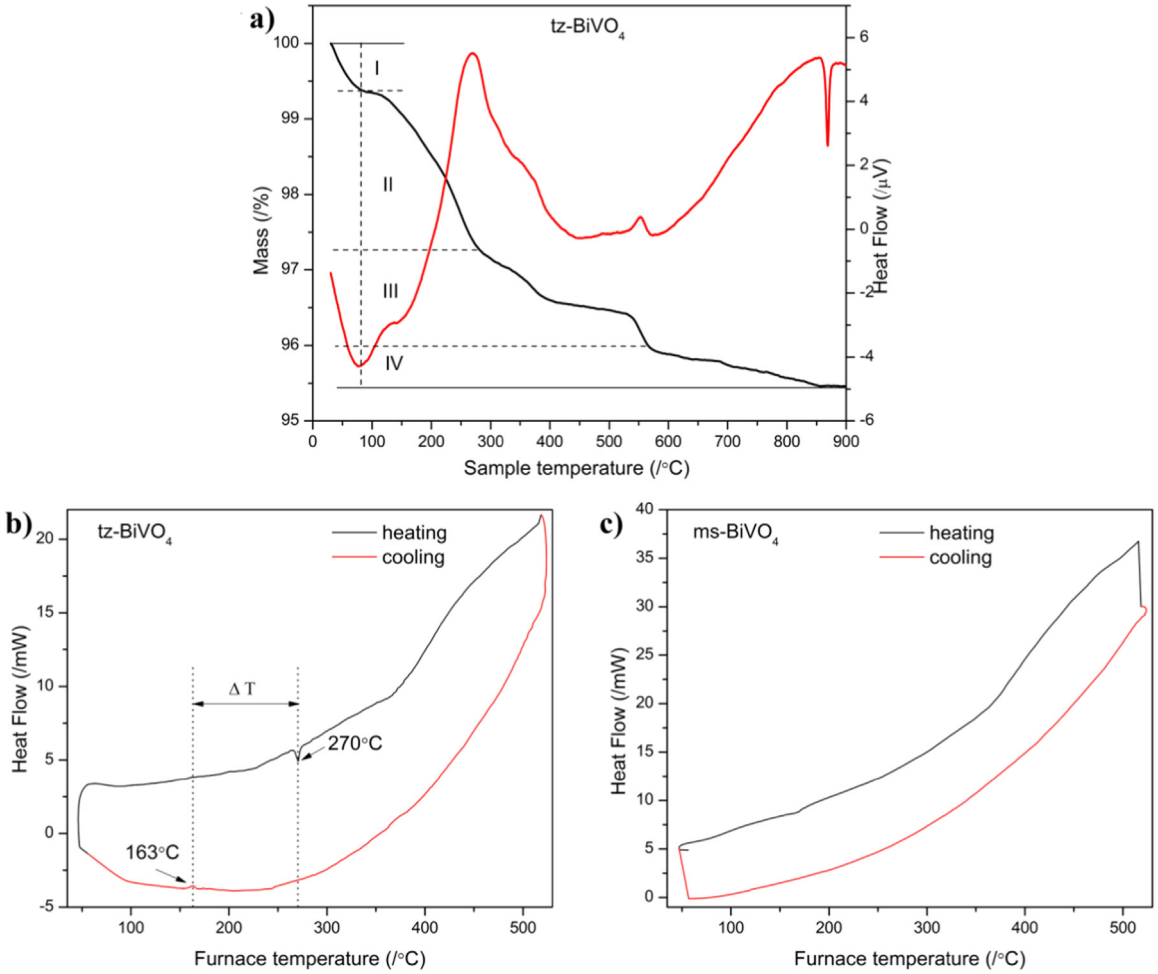

Fig. 4. a)TGA/DTA curves and DSC curves for b) *tz*-$BiVO_4$-1A and c) *ms*-$BiVO_4$-1A-450 nanoparticles between 20 °C and 500 °C with a heating/cooling rate of 10 °C min^{-1}.

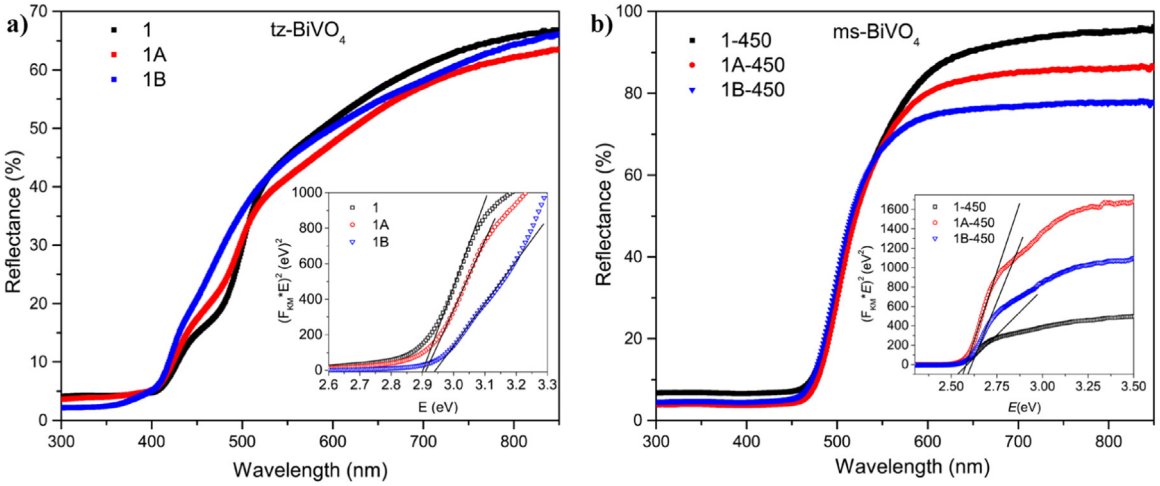

Fig. 5. UV–visible diffusive reflectance spectra of: a) *tz*-$BiVO_4$ and b) *ms*-$BiVO_4$ nanoparticles; insets show Kubelka-Munk plots and estimations of band-gap energies.

endothermic peaks observed at about 77, 150, 570 and 870 °C and two exothermic peaks at about 270 °C and 550 °C.

Peak from DTA curve at 850 °C corresponds to the melting point of $BiVO_4$. The phase changes of *tz*-$BiVO_4$ and *ms*-$BiVO_4$ samples were studied by differential scanning calorimetry (DSC) as shown in Fig. 4b and c.

Main difference between the DSC curves for *tz*-$BiVO_4$ and *ms*-$BiVO_4$ nanoparticles is the appearance of endothermic and exothermic peaks at different temperatures during heating-cooling processes in *tz*-$BiVO_4$ nanoparticles compared with the *ms*-$BiVO_4$ nanoparticles.

The phenomenon is so-called thermal hysteresis and it is equivalent to the difference between the temperatures of maximal endothermic peak during heating (T_h = 270 °C) and maximal exothermic peak during cooling (T_c = 163 °C), i.e. $\Delta T = T_h - T_c$ = 107 °C. Thermal

hysteresis occurs in these samples because the transitions between various structure phases occur at different temperatures for both the heating and cooling processes. This phenomenon does not occur often and could be attributed to the size of the nanoparticles. Namely, as we discussed above, *tz*-$BiVO_4$ nanoparticles have diameters in range 5–10 nm, while *ms*-$BiVO_4$ polycrystalline nanoparticles could be referred to as bulk material. It is in full agreement with literature reports of ellipsoidal $BiVO_4$ expressing the phenomenon of thermal hysteresis compared to the bulk $BiVO_4$ nanoparticles [20]. In bulk *ms*-$BiVO_4$ nanoparticles this phenomenon does not appear due to irreversible monoclinic structure phase switch occurring at about 500 °C.

3.3. Optical properties of *tz*-$BiVO_4$ and *ms*-$BiVO_4$ nanoparticles

3.3.1. UV–Vis diffuse reflectance spectra

Fig. 5 shows the UV–visible diffuse reflectance spectra of the $BiVO_4$ powders with different structures. All the samples exhibited a strong absorption band in the near UV region and had a steep absorption edge. Spectra of *ms*-$BiVO_4$ (Fig. 5(b)) show that the absorption was extended to the visible light region. The steep absorption edge suggests that the observed absorption is not caused by transitions involving impurity levels (impurity-to-band, band-to-impurity, or impurity-to-impurity transitions). Thus, it may be attributed to band-to-band electronic transitions from the top of the valance band to the bottom of the conduction band. The band gap, E_g, was estimated from the spectra according to the following equation:

$$(F_{KM} \times h\nu)^{1/n} = A(h\nu - E_g) \quad (1)$$

where F_{KM} is the Kubelka–Munk function, with $F_{KM}(R) = (1 - R)^2/(2R)$, where R is the observed reflectance, A is a constant and $E = h\nu$ is the photon energy. The values of n for direct allowed, indirect allowed and direct forbidden transitions are n = 1/2, 2, and 3/2, respectively. $BiVO_4$ is a direct gap semiconductor, therefore n = 1/2. According to Eq. (1), a corresponding band gap value, Eg, was determined from a plot of $(F_{KM} \times E)^2$ versus incident light energy E by extrapolating the steepest portion of the graph to where it intersected the E axis. As shown in the insets of Fig. 5, the calculated band gap energies are: 2.90 eV, 2.91 eV and 2.94 eV for *tz*-$BiVO_4$-1, 1A and 1B, and 2.53 eV, 2.56 eV and 2.59 eV for *ms*-$BiVO_4$-1-450, 1A-450 and 1B-450, respectively. Note that in the case of *ms*-$BiVO_4$, E_g is somewhat larger than the value reported for the bulk material (2.40 eV), while the band gap energies of *tz*-$BiVO_4$ are in a good agreement with the data previously reported [3].

3.4. Photocatalytic/adsorptive performance of *tz*-$BiVO_4$ and *ms*-$BiVO_4$ nanoparticles

3.4.1. Adsorption isotherms (BET experiments)

Nitrogen adsorption/desorption isotherms (Fig. 6) at temperature of liquid nitrogen (-196°C) for *tz*-$BiVO_4$ and *ms*-$BiVO_4$ were measured, and isotherm data for each powder were used to estimate specific surface area, average pore size, pore size distribution, mesopore surface area, micropore volume and mesopore volume. All samples showed a type IV isotherm curve with an H3 hysteresis loop according to IUPAC (the International Union of Pure and Applied Chemistry) classification, which is indicative of a mesoporous material [18,21]. Note that, in terms of the IUPAC nomenclature, porous materials are classified as microporous (pore diameter < 2 nm), mesoporous (2 nm < pore diameter < 50 nm), and macroporous (pore diameter > 50 nm). Adsorption/desorption isotherms on *tz*-$BiVO_4$ are presented in Fig. 6 as an illustration of N_2 adsorption measurements.

Values of the specific surface area (S_{BET}) of all the synthesized materials, calculated by means of the BET method, are listed in Table 2. Pore size distributions were estimated from the adsorption branch of the N_2 isotherms using the Barrett- Joyner-Halenda model. It was found

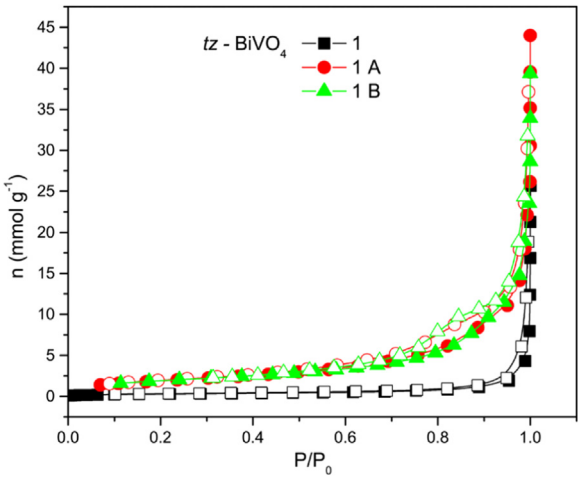

Fig. 6. Nitrogen adsorption/desorption isotherm curves (solid symbols – adsorption, open symbols – desorption) of the *tz*-$BiVO_4$ samples.

Table 2
Porous properties of synthesized *tz*- and *ms*-$BiVO_4$ samples.

Sample		S_{BET} (m^2/g) S_{meso} (m^2/g)	r_{med} (nm)
1	*tz*-$BiVO_4$	5	9.0
1A		34	4.6
1B		32	5.0
1-450	*ms*-$BiVO_4$	5	9.7
1A-450		10	11.2
1B-450		7	10.3

that the studied samples were mesoporous regardless of their crystalline structure (see Table 2 for values of mean pore radius, r_{med}) and in the case of *tz*-$BiVO_4$ with most pores in radii from 2 to 10 nm.

For *ms*-$BiVO_4$ (the samples 1A-450 and 1B-450) photocatalysts, thermal treatment at 450 °C caused the decreases in surface area and the increase in r_{med}, as expected. The conclusions regarding mesoporosity were further confirmed by an additional t-plot analysis showing that there was no microporosity present in any of the samples. The t-plot method provides estimates for micropore volume (V_{mic}), mesopore surface area (external surface area, S_{meso}), and micropore surface area (S_{mic}; $S_{mic} = S_{BET} - S_{meso}$) (see Table 2). Values of V_{mic} and S_{meso} were calculated from the intercept and slope of the straight line in the t-plot, respectively.

Most *ms*-$BiVO_4$ materials studied in the last 20 years were mainly composed of macroparticles and made by various methods with BET surface area values in the range of 1–8 m^2/g. Note that 0.72 m^2/g was measured for bulk *ms*-$BiVO_4$ synthesized by a solid-state method [19,20]. In this work, the nanostructured *ms*-$BiVO_4$ samples exhibited surface areas in accordance with those found in the literature for nanosized powders: Ressnig et al. (7.4 m^2/g) [22], Sun et al. (0.7–10.4 m^2/g) [23], Hofmann et al. (7–16 m^2/g) [24] and Luo et al. (10–17 m^2/g) [25]. Zircon-type $BiVO_4$ has not been studied in a systematic way and only a few values of the specific area are available in the literature: 1.24 m^2/g [8], 3 m^2/g [9], 2.3 m^2/g [26], 4.47 m^2/g [27] and 5 m^2/g [15]. However, for *tz*-$BiVO_4$ prepared here by a novel synthetic approach, a remarkable increase in measured surface area S_{BET} was observed: 32 m^2/g and 34 m^2/g, which is 45–47 times larger than that of the bulk *ms*-$BiVO_4$.

3.4.2. Photocatalytic performance

It has been generally accepted that photocatalytic performance of a semiconducting material is influenced by many factors: its structure, surface properties, energy bandgap, crystalline structure, crystallinity,

particles size and morphology, porosity, and porous texture (surface area, pore size and pore size distribution). Earlier reports indicate that the photocatalytic activity of $BiVO_4$ largely depends on the crystalline phases, specific surface area and the transport properties of photo-induced charge carriers. [13] Mesoporous materials, whose pore size range from 2 to 50 nm, are of interest because of their potential use in various fields including heterogeneous catalysis, energy, biotechnology, and nano-devices. Because of their high specific surface area and pore size, mesoporous materials are also promising adsorbents for removal of organic pollutants from aqueous solution.

Adsorptive and photocatalytic activity of $BiVO_4$ nanocrystalline powders synthesized through an ethylene glycol route at room temperature was evaluated by adsorptive removal and photocatalytic degradation of methyl orange (MO). The initial dye concentration (C_0) was 5 mg/dm^3. At certain time intervals, the residual MO concentration (C) was spectrophotometrically measured at the characteristic absorption maximum of 464 nm arising from the "–N=N–" azo bonding. Plot of relative concentration of MO (i.e. C/C_0 ratio) against a treatment time t describes kinetics of the dye removal from a suspension of a $BiVO_4$ catalyst powder and an aqueous solution of the dye. The quantity $(C_0 - C)/C_0 = 1–C/C_0$, which is usually expressed as a percentage $(100 \times (C_0 - C)/C_0)$, is called a removal (photocatalytic, or degradation) efficiency. Decolourization of MO was examined under two different experimental conditions: either there was no illumination and the $BiVO_4$-based photocatalyst was present, or the photocatalyst was utilized under light illumination. An artificial light source (Osram Ultra-Vitalux, 300 W) with a sun-like radiation spectrum from 280 to 1800 nm was used for illumination. Initial tests in the absence of the catalyst and under light exposure showed negligible degradation of the dye.

Adsorption experiments were carried out in the dark before photodegradation experiments. For both *tz*-$BiVO_4$ and *ms*-$BiVO_4$ powders, adsorption-desorption equilibrium of the dye on the catalyst surface was achieved within 180 min. It was found that adsorption levels were around 20% for all *tz*-$BiVO_4$ nanoparticles, whereas all *ms*-$BiVO_4$ samples exhibited negligible adsorption of MO. It is noteworthy that in either case adsorptive activity did not reflect changes in porosity. For all the samples, after adsorption equilibrium was reached, the zero time reading was chosen and then the dye solution with catalyst was exposed to UV–Vis light irradiation. Fig. 7a depicts the experimental data on the time-dependent photocatalytic removal of MO over different *tz*-$BiVO_4$ nanoparticles. As can be seen from the photocatalytic degradation curves, a contact time of 240 min was sufficient to achieve a removal efficiency of 100% in all photocatalytic activity tests. In Fig. 7b, a decrease in the absorption maximum of *tz*-$BiVO_4$-1A indicating a rapid degradation of the dye is presented.

The kinetics of degradation was approached using the Langmuir-Hinshelwood model (when the initial adsorbate concentration is low) and the pseudo-first-order kinetics. The experimental kinetic data were fitted to pseudo-first-order kinetic equation in its integrated form: $\ln(C_0/C) = k_{app}\, t$, where C_0 is the initial MO concentration, C is the concentration at reaction time t and k_{app} is the (apparent) rate constant [28]. For the samples 1, 1A and 1B, by the linear regression analysis (with intercept = 0), the k_{app} (min^{-1}) values (along with regression R^2-squared values) were estimated to be 0.016 (0.941), 0.033 (0.994) and 0.018 (0.996) respectively. Overall, the *tz*-$BiVO_4$-1A sample showed greatest activity and observed differences in efficiency among the three samples were consistent with changes in a specific surface area. However, the difference between *tz*-$BiVO_4$-1 and *tz*-$BiVO_4$-1B was not as great as would have been expected from a change in S_{BET} alone.

Clearly, this and other experimental findings presented here require a systematic and detailed study. These first results, however, indicate that the optimized tetragonal zircon-type-$BiVO_4$ exhibited a markedly good performance with respect to MO removal and it would be interesting to examine it further for use in water and wastewater treatments [29,30].

To characterize the overall performance of a photocatalyst, consideration should be given not just to its activity, but to reusability features as well. Since *tz*-$BiVO_4$-1A showed best efficiency in removing the MO from solutions of the dye, its reusability was studied. The extent of reusability was determined by reusing the catalyst for subsequent photodegradation experiments. Between the two successive photocatalytic experiments, used powder of *tz*-$BiVO_4$-1A was washed several times with water and buffer solutions and dried at 110 °C for 24 h. Afterwards, the powder was homogenized and submitted to yet another photocatalytic experiment of MO degradation. As Fig. 8 shows, there was no significant decrease of activity not even after the fifth use.

In our tests, nanosized *ms*-$BiVO_4$ (with specific surface area 5–10 m^2/g) showed less catalytic degradation efficiency under UV–Vis illumination. The time-dependent dye decolorization of MO solution over all monoclinic scheelite-type materials and UV–Vis absorption spectra of MO (over *ms*-$BiVO_4$-1A) are given in Fig. 9. The removal efficiency of 30–35% was observed for all prepared catalysts. It was found that all tested *ms*-$BiVO_4$ samples exhibited a good reusability; there was no significant loss of photocatalytic activity of *ms*-$BiVO_4$-1A powder over three consecutive degradation cycles. The diminution of activity was around 3%.

Finally, FTIR analysis showed that there was no MO adsorbed on the catalyst surface (representative spectra are given in Fig. 10), which leads us to conclusion that MO was adsorbed inside mesoporous structure of the *tz*-$BiVO_4$. A very strong absorption band at 742 cm^{-1}

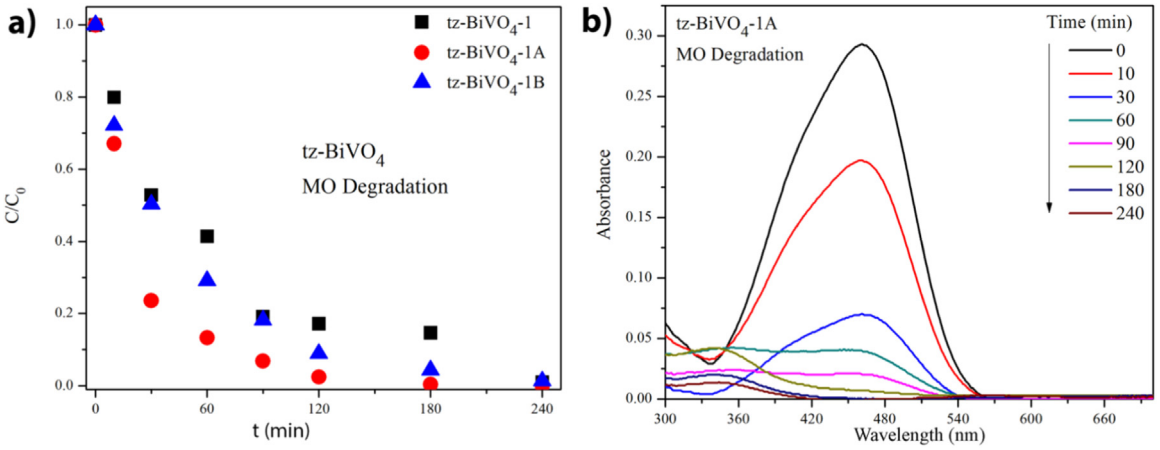

Fig. 7. a) Photocatalytic degradation curves of MO solution (5 mg/L) over different *tz*-$BiVO_4$ samples (1 g/L) under UV–Vis light irradiation. C_0 and C_t are the concentrations of MO before irradiation and after it is irradiated for t min, respectively. b) Time dependence of the UV absorption spectrum of MO dye in the aqueous suspension of *tz*-$BiVO_4$-1A.

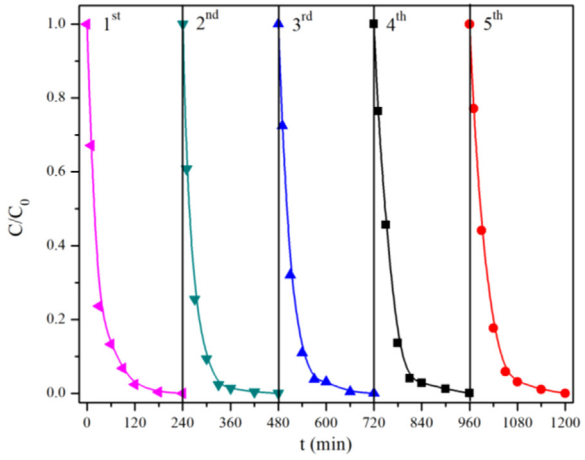

Fig. 8. Reusability of *tz*-$BiVO_4$-1A powder.

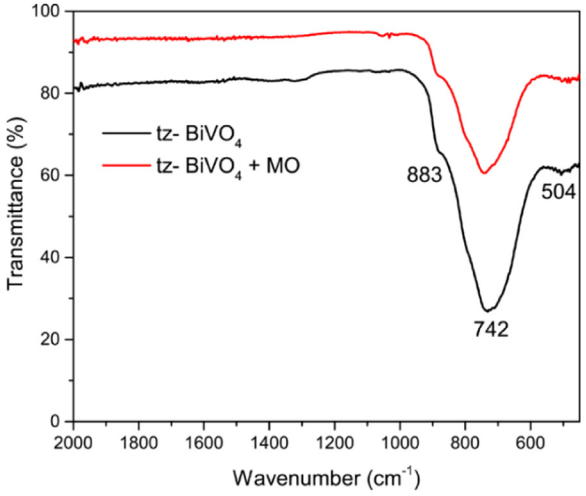

Fig. 10. FTIR spectra of *tz*-$BiVO_4$-1A powder and *tz*-$BiVO_4$-1A powder after photodegradation experiment.

with a shoulder at 883 cm^{-1} is associated with stretching modes (asymmetric and symmetric) corresponding to the V–O bond, while an absorption band at 504 cm^{-1} could be ascribed to bending of the vanadate anion VO_4^{3-} [8,31].

The above results show that pure *tz*-$BiVO_4$ performed better than *ms*-$BiVO_4$ in both adsorption and photocatalytic degradation experiments. In particular, the *tz*-$BiVO_4$-1A sample displayed enhanced photocatalytic activity indicating that MO solution could be effectively decolorized under UV–Vis light. These initial results suggest that optimized zircon-type $BiVO_4$ may be used as a suspension-type photocatalyst for organic pollutants in aqueous environment. However, as far as we are aware, it seems that no such experimental data have been reported before. As a matter of fact, in few available photocatalytic studies [9,10,13–16] chemically pure single-phase *tz*-$BiVO_4$ was found to be a very poor photocatalyst. Only according to one report, it exhibited better adsorption performance (for methyl blue) than *ms*-$BiVO_4$ [10], but its overall activity was significantly lower. Further, although better photocatalytic performance of tetragonal $BiVO_4$ compared to the monoclinic one was stated in Conclusions of [32], the sample under investigation, in fact, was *tz*/*ms* composite $BiVO_4$ (95% of tetragonal phase).

It should be remarked that using dyes to assess the photocatalytic efficiency is not that straightforward and could be problematic [33]. However, although the dye degradation tests are significantly influenced by various factors and may suffer from some serious drawbacks and limitations, such as difficulty to distinguish between photocatalytic and photosensitization processes, they are inexpensive and their simplicity, easiness of use and rapidity are yet of great advantage. For these reasons, photodegradation was here utilized for first estimates of photocatalytic performance. In any case, these intriguing experimental findings were encouraging enough and clearly merit further, more elaborate investigation. It is noteworthy that tetragonal scheelite-type $BiVO_4$, *ts*-$BiVO_4$, the third of three commonly found polymorphs of bismuth vanadate, was recently shown to be moderately photocatalytically active [9] although quite the opposite was suggested in the first reports [10,12].

4. Conclusions

As is it can be evidenced by an exponential growth in the number of publications over the past decade, monoclinic scheelite-type $BiVO_4$ has attracted considerable research attention as a promising photocatalyst. However, tetragonal zircon-type $BiVO_4$ is still poorly understood and, here, our aims were to develop a novel low-temperature synthesis of nanostructured single-phase *tz*-$BiVO_4$ in a non-aqueous medium and to determine whether or not the new synthetic approach to *tz*-$BiVO_4$ influences its adsorption and/or photocatalytic performance (see Introduction).

To prepare nanostructured zircon-type $BiVO_4$ in a non-aqueous medium, a simple, non-conventional and easily scalable process was

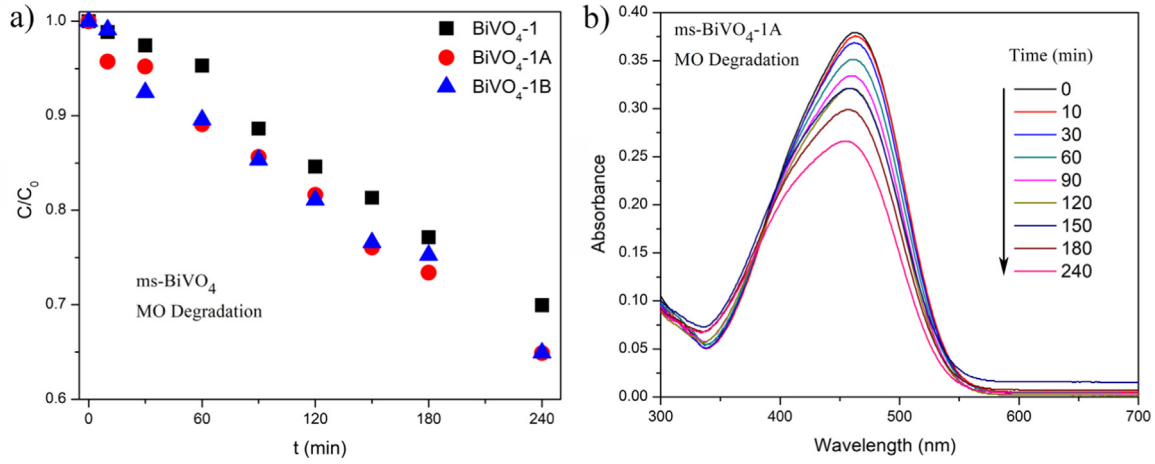

Fig. 9. a) Photocatalytic degradation curves of MO solution (5 mg/L) over different *ms*-$BiVO_4$ (1 g/L) samples under UV–Vis light irradiation. b) Time dependence of the UV absorption spectra of MO dye in the aqueous suspension of *ms*-$BiVO_4$-1A.

proposed. A controllable ethylene-glycol colloidal route at room temperature was for the first time utilized to successfully synthesize powdered *tz*-$BiVO_4$. XRD patterns of the obtained powders clearly showed presence of a pure single tetragonal zircon-type crystalline phase, while nanocrystals (5–10 nm in size) were revealed by TEM images. In addition, because of the irreversible tetragonal-to-monoclinic transition, it was possible to easily obtain powdered *ms*-$BiVO_4$ by annealing the as-prepared samples at 450 °C for 24 h. A pure single monoclinic scheelite-type phase was identified in all the annealed powders, while the average particle sizes found by TEM analysis (20–60 nm) were larger than those of the crystallites (estimated from the XRD patterns).

Crystalline phase effects on thermal and optical properties as well as on adsorption and photocatalytic activity were studied for both the as-prepared and annealed materials. To assess the extent to which the new way of preparation of *tz*-$BiVO_4$ influenced its adsorption and photocatalytic performance, for all *tz*-$BiVO_4$ and *ms*-$BiVO_4$ samples, nitrogen adsorption-desorption analysis was carried out and photocatalytic activity was evaluated by degradation of methyl orange in an aqueous solution.

It was found that the new synthetic approach to *tz*-$BiVO_4$ had a significant effect on its porosity and photocatalytic activity towards degradation of MO solution. All the prepared materials were mesoporous and for some *tz*-$BiVO_4$ powders a remarkable increase in measured surface area S_{BET} was observed: 32 m^2/g and 34 m^2/g, which is 45–47 times larger than that of the bulk *ms*-$BiVO_4$, or ~7 times higher than that reported thus far for this phase. Also, *tz*-$BiVO_4$ showed better overall performance than *ms*-$BiVO_4$ in adsorption/photocatalytic experiments of methyl orange degradation under sun-like illumination. To the best of our knowledge, it seems that such findings, particularly enhanced and better photocatalytic performance of tetragonal zircon-type $BiVO_4$, were never reported before in the open literature. It could be expected, therefore, that the present preparation method and initial experimental observations of an ongoing research will both arouse interest in scarcely studied tetragonal zircon-structured $BiVO_4$ and facilitate as well as speed up further research of its properties.

Acknowledgements

The authors from Vinča Institute of Nuclear Sciences acknowledge the financial support of the Ministry of Education, Science and Technological Development of the Republic of Serbia (Project no: 172056). The work of K. Smits was supported by Latvian National Research Program IMIS2 (Grant no. 302/2012).

References

[1] Y. Park, K.J. McDonald, K.-S. Choi, Progress in bismuth vanadate photoanodes for use in solar water oxidation, Chem. Soc. Rev. 42 (2013) 2321–2337.
[2] N.R. Khalid, A. Majid, M. Bilal Tahir, N.A. Niaz, S. Khalid, Carbonaceous-TiO_2 nanomaterials for photocatalytic degradation of pollutants: a review, Ceram. Int. 43 (2017) 14552–14571.
[3] Z. Li, W. Luo, M. Zhang, J. Feng, Z. Zou, Photoelectrochemical cells for solar hydrogen production: current state of promising photoelectrodes, methods to improve their properties, and outlook, Energy Environ. Sci. 6 (2013) 347–370.
[4] J.H. Sun, H. Yang, A polyacrylamide gel route to photocatalytically active $BiVO_4$ particles with monoclinic scheelite structure, Ceram. Int. 40 (2014) 6399–6404.
[5] K. Zhang, J. Deng, Y. Liu, S. Xie, H. Dai, In Semiconductor photocatalysis - materials, mechanisms and applications (Chapter 21), in: W. Cao (Ed.), Photocatalytic Removal of Organics over $BiVO_4$-Based Photocatalysts, In Tech, Rijeka, 2016.
[6] Y. Zhao, R. Li, L. Mu, C. Li, Significance of crystal morphology controlling in semiconductor-based photocatalysis: a case study on $BiVO_4$ photocatalyst, Cryst. Growth Des. 6 (2017) 2923–2928.
[7] W. Ma, Z. Li, W. Liu, Hydrothermal preparation of $BiVO_4$ photocatalyst with perforated hollow morphology and its performance on methylene blue degradation, Ceram. Int. 41 (2015) 4340–4347.
[8] G.P. Nagabhushana, A.H. Tavakoli, A. Navrotsky, Energetics of bismuth vanadate, J. Solid State Chem. 225 (2015) 187–192.
[9] T. Saison, N. Chemin, C. Chanéac, O. Durupthy, L. Mariey, F. Maugé, V. Brezová, J.-P. Jolivet, New insights into $BiVO_4$ properties as visible light photocatalyst, J. Phys. Chem. C. 119 (2015) 12967–12977.
[10] A. Iwase, H. Kato, A. Kudo, A simple preparation method of visible-light-driven $BiVO_4$ photocatalysts from oxide starting materials (Bi_2O_3 and V_2O_5) and their photocatalytic activities, J. Sol. Energy Eng. 132 (2010) 21106 (10pp).
[11] A.K. Bhattacharya, K.K. Mallick, A. Hartridge, Phase transition in $BiVO_4$, Mater. Lett. 30 (1997) 7–13.
[12] G. Li, Y. Bai, W.F. Zhang, Difference in valence band top of $BiVO_4$ with different crystal structure, Mater. Chem. Phys. 136 (2012) 930–934.
[13] H. Fan, T. Jiang, H. Li, D. Wang, L. Wang, J. Zhai, D. He, P. Wang, T. Xie, Effect of $BiVO_4$ crystalline phases on the photoinduced carriers behavior and photocatalytic activity, J. Phys. Chem. C. 116 (2012) 2425–2430.
[14] X. Zhang, Z. Ai, F. Jia, L. Zhang, X. Fan, Z. Zou, Selective synthesis and visible-light photocatalytic activities of $BiVO_4$ with different crystalline phases, Mater. Chem. Phys. 103 (2007) 162–167.
[15] S. Obregon, G. Colon, Improved O_2 evolution from a water splitting reaction over Er^{3+} and Y^{3+} co-doped tetragonal $BiVO_4$, Catal. Sci. Technol. 4 (2014) 2042–2050.
[16] H.M. Zhang, J.B. Liu, H. Wang, W.X. Zhang, H. Yan, Rapid microwave-assisted synthesis of phase controlled $BiVO_4$ nanocrystals and research on photocatalytic properties under visible light irradiation, J. Nanopart. Res. 10 (2008) 767–774.
[17] D.D. Do, Adsorption Analysis: Equilibria and Kinetics, Imperial College Press, 1998.
[18] S. Lowell, J.E. Shields, M.A. Thomas, M. Thommes, Characterization of Porous Solids and Powders: Surface Area, Pore Size and Density, Kluwer Academic Publishers, Dordrecht Netherlands, 2004, p. 44.
[19] Y. Sun, Y. Xie, C. Wu, S. Zhang, S. Jiang, Aqueous synthesis of mesostructured $BiVO_4$ quantum tubes with excellent dual response to visible light and temperature, Nano Res. 3 (2010) 620–631.
[20] Y. Sun, C. Wu, R. Long, Y. Cui, S. Zhang, Y. Xie, Synthetic loosely packed monoclinic $BiVO_4$ nanoellipsoids with novel multiresponses to visible light, trace gas and temperature, Chem. Commun. 30 (2009) 4542–4544.
[21] K.S.W. Sing, D.H. Everett, R. A.W. Haul, L. Moscou, R.A. Pierotti, J. Rouquérol, T. Siemieniewska, Reporting physisorption data for gas/solid systems with special reference to the determination of surface area and porosity, Pure Appl. Chem. 57 (1985) 603–619.
[22] D. Ressnig, R. Kontic, G.R. Patzke, Morphology control of $BiVO_4$ photocatalysts: pH optimization vs. self-organization, Mater. Chem. Phys. 135 (2012) 457–466.
[23] W. Sun, M. Xie, L. Jing, Y. Luan, H. Fu, Synthesis of large surface area nano-sized $BiVO_4$ by an EDTA-modified hydrothermal process and its enhanced visible photocatalytic activity, J. Solid State Chem. 184 (2011) 3050–3054.
[24] M. Hofmann, M. Rainer, S. Schulze, M. Hietschold, M. Mehring, Nonaqueous synthesis of a bismuth vanadate photocatalyst by using microwave heating: photooxidation versus photosensitized decomposition in visible-light-driven photocatalysis, ChemCatChem 7 (2015) 1357–1365.
[25] Q. Luo, L. Zhang, X. Chen, O.K. Tan, K.C. Leong, Mechanochemically synthesized m-$BiVO_4$ nanoparticles for visible light photocatalysis, RSC Adv. 6 (2016) 15796–15802.
[26] Z. Wang, W. Luo, S. Yan, J. Feng, Z. Zhao, Y. Zhu, Z. Li, Z. Zou, $BiVO_4$ nano-leaves: mild synthesis and improved photocatalytic activity for O_2 production under visible light irradiation, CrystEngComm 13 (2011) 2500–2504.
[27] W. Li, X. Wang, Z. Wang, Y. Meng, X. Sun, T. Yan, J. You, D. Kong, Relationship between crystalline phases and photocatalytic activities of $BiVO_4$, Mater. Res. Bull. 83 (2016) 259–267.
[28] M.N. Chong, B. Jin, C.W.K. Chow, C. Saint, Recent developments in photocatalytic water treatment technology: a review, Water Res. 44 (2010) 2997–3027.
[29] A. Arshad, J. Iqbal, I. Ahmad, M. Israr, Graphene/Fe_3O_4 nanocomposite: interplay between photo-Fenton type reaction, and carbon purity for the removal of methyl orange, Ceram. Int. 44 (2018) 2643–2648.
[30] N. Li, B. Yang, L. Xu, G. Xu, W. Sun, S. Yu, Simple synthesis of Cu_2O/Na-bentonite composites and their excellent photocatalytic properties in treating methyl orange solution, Ceram. Int. 42 (2016) 5979–5984.
[31] G. Socrates, Infrared and Raman Characteristic Group Frequencies: Table and Charts, 3rd ed., Jon Wiley and Sons, New York, 2001.
[32] S. Obregón, S.W. Lee, G. Colón, Exalted photocatalytic activity of tetragonal $BiVO_4$ by Er^{3+} doping through a luminescence cooperative mechanism, Dalton Trans. 43 (2014) 311–316.
[33] N. Barbero, D. Vione, Why dyes should not be used to test the photocatalytic activity of semiconductor oxides, Environ. Sci. Technol. 50 (2016) 2130–2131.